



# Boosting selectivity and stability on Pt/BN catalysts for propane dehydrogenation via calcination & reduction-mediated strong metal-support interaction

Yaoxin Wang<sup>1</sup>, Jiandian Wang<sup>1</sup>, Ping Zheng<sup>1</sup>, Changyong Sun<sup>\*</sup>, Junyin Luo, Xiaowei Xie<sup>\*</sup>

Key Laboratory of Clean Chemical Technology of Guangdong Regular Higher Education Institutions, School of Chemical Engineering and Light Industry, Guangdong University of Technology, Guangzhou 510006, Guangdong, China

## ARTICLE INFO

### Article history:

Received 21 August 2021

Revised 24 September 2021

Accepted 4 October 2021

Available online 26 October 2021

### Keywords:

Pt catalyst

BN

SMSI

Propane dehydrogenation

Selectivity

Stability

Coke

Sintering

## ABSTRACT

Propane dehydrogenation (PDH) provides an alternative route for producing propylene. Herein, we demonstrate that h-BN is a promising support of Pt-based catalysts for PDH. The Pt catalysts supported on h-BN were prepared by an impregnation method using  $\text{Pt}(\text{NH}_3)_4(\text{NO}_3)_2$  as metal precursors. It has been found that the Pt/BN catalyst undergoing calcination and reduction is highly stable in both PDH reaction and coke-burning regeneration, together with low coke deposition and outstanding propylene selectivity (99%). Detailed characterizations reveal that the high coke resistance and high propylene selectivity of the Pt/BN catalyst are derived not only from the absence of acidity on BN support, but also from the calcination-induced and reduction-adjusted strong metal-support interaction (SMSI) between Pt and BN, which causes the partial encapsulation of Pt particles by  $\text{BO}_x$  overlayers. The  $\text{BO}_x$  overlayers can block the low-coordinated Pt sites and constrain Pt particles into smaller ensembles, suppressing side reactions such as cracking and deep dehydrogenation. Moreover, the  $\text{BO}_x$  overlayers can effectively inhibit Pt sintering by the spatial isolation of Pt during periodic reaction-regeneration cycles. In this work, the catalyst support for PDH is expanded to nonoxide BN, and the understanding of SMSI between Pt and BN will provide rational design strategy for BN-based catalysts.

© 2021 Science Press and Dalian Institute of Chemical Physics, Chinese Academy of Sciences. Published by ELSEVIER B.V. and Science Press. All rights reserved.

## 1. Introduction

Due to the growing demand of propylene as an important base chemical intermediate and the increasing production of propane from shale gas in the past few years, the catalytic dehydrogenation of propane draws more attention as an alternative route for producing propylene [1–5]. Similar to the case of other light paraffin dehydrogenation reactions, propane dehydrogenation can be operated under nonoxidative [6,7] or oxidative conditions [8,9]. Oxidative dehydrogenation of propane (ODHP) overcomes equilibrium limitations and avoids thermal cracking, but it suffers from relatively low selectivity to propylene. To date, nonoxidative propane dehydrogenation (PDH) is the main approach in large-scale commercial applications. However, PDH is endothermic and equilibrium-limited, necessitating high temperatures to achieve high per-pass conversion of propane, which often causes rapid cat-

alyst deactivation and decreased selectivity. It is always a challenge to develop highly stable and highly selective catalysts for PDH.

Platinum is the most frequently used as an active metal in PDH due to its superior activation of C–H bonds, low activity to C–C cleavage, and environment-friendly property [1]. The major issue of Pt-based catalysts in PDH is rapid deactivation caused by coke formation and metal agglomeration. Hence, many efforts have been devoted to enhancing catalytic stability of Pt-based catalysts. Adding promoters, such as Sn [10–13] and Zn [14–17], has been proved helpful to suppress coke formation and inhibit metal sintering, as well as to increase propylene selectivity. The role of promoters is ascribed to the generation of alloyed Pt or the interaction with Pt in close proximity. On the other hand, the support also plays an important role in determining the dispersion, stability, and structural and electronic properties of Pt. Alumina is the classical support employed to support Pt in PDH, where the acid sites on alumina can efficiently disperse Pt, but lead to a significant amount of coke deposition. Compared with alumina support, weakly acidic or nonacidic supports, such as MgAl-based layered

<sup>\*</sup> Corresponding authors.

E-mail addresses: [chysun@gdut.edu.cn](mailto:chysun@gdut.edu.cn) (C. Sun), [xwxie@gdut.edu.cn](mailto:xwxie@gdut.edu.cn) (X. Xie).

<sup>1</sup> These authors contributed equally to this work.

double hydroxides [16,18] and purely siliceous zeolites [12,14,17], can curb coking, showing better performance in PDH.

Due to the large thermal conductivity, superior temperature stability, excellent acid-base resistance, and specific coordinatively unsaturated edge sites, hexagonal boron nitride (h-BN) has been used as a support of supported catalysts in various catalytic reactions [19–23]. It has also been reported that h-BN as a coating material of core-shell catalysts can tune the surface reactivity of the core metals [24–26]. In particular, the oxygen species or hydroxyl linked to boron atoms at layer edges enable h-BN to catalyze the ODHP [27,28] or styrene epoxidation [29] as a catalyst. In our previous work [30], it was found that h-BN can effectively disperse and stabilize Pt as a catalyst support. Considering that BN is not acidic and of high thermal stability, it can be inferred that the BN-supported Pt may have low coke formation and high stability in PDH. Herein, we show an investigation on the dehydrogenation of propane over the BN-supported Pt catalysts. A 0.5 wt% Pt/BN catalyst, undergoing calcination in air and reduction in hydrogen, has been proved highly selective to propylene and highly stable in consecutive reaction-regeneration cycles. Detailed characterizations demonstrate that the strong metal-support interaction (SMSI) induced by calcination and adjusted by reduction is responsible for the high selectivity and stability of Pt/BN in PDH.

## 2. Experimental

### 2.1. Catalyst preparation

The Pt/BN catalyst with a targeted Pt loading of 0.5 wt% was prepared by impregnating h-BN ( $\sim 25 \text{ m}^2 \text{ g}^{-1}$ , Aladdin, Shanghai) with aqueous  $\text{Pt}(\text{NH}_3)_4(\text{NO}_3)_2$  (Sino-Platinum, Kunming) solution. After stirring well, the impregnation mixture was dried by rotary evaporator at  $50^\circ\text{C}$  for 2 h, and further dried in an oven at  $110^\circ\text{C}$  overnight. Finally, the catalyst was calcined in a muffle at  $600^\circ\text{C}$  for 4 h and then pressed into pellets with 60–80 mesh. Note, in some cases, the calcination treatment was left out or the calcination temperature was changed. Before some characterization tests, where the catalyst cannot be reduced *in situ*, the calcined catalyst was prereduced in a 10 vol%  $\text{H}_2/\text{N}_2$  atmosphere at  $550^\circ\text{C}$ . For comparison, the  $\text{Pt}/\text{Al}_2\text{O}_3$  catalyst was prepared by the same procedure as the Pt/BN catalyst.

### 2.2. Characterizations

The Pt content was measured by the atomic absorption spectroscopy (AAS) technique on a Shimadzu AA-6880. X-ray powder diffraction (XRD) measurement was conducted on a Rigaku Ultima IV diffractometer using  $\text{Cu K}_\alpha$  radiation operated at 40 kV and 40 mA. Transmission electron microscopy (TEM), high-resolution transmission electron microscopy (HRTEM), and high-angle annular dark-field scanning transmission electron microscopy (HAADF-STEM) images were taken on an FEI Tecnai G2F30 or G220 microscope using different modes with the maximum operating voltage of 200 kV. The specimen was prepared by ultrasonically dispersing the sample powder in ethanol, and drops of the suspension were deposited on a carbon-coated copper grid and dried in air.

X-ray photoelectron spectroscopy (XPS) data were collected by a Thermo Fisher Escalab 250Xi using monochromatic Al  $K_\alpha$  X-ray under ultrahigh vacuum condition ( $<5 \times 10^{-10} \text{ mbar}$ ). An additional pretreatment chamber allowed *in situ* calcination/reduction and transfer of the sample. The adventitious carbon 1 s peak was calibrated at 284.8 eV to compensate for any charging effects.

Pulse CO-chemisorption and temperature-programmed oxidation (TPO) were carried out on a Hiden Catlab equipped with a QGA mass spectrometer. Before pulse chemisorption, the catalyst

was calcined and/or reduced *in situ*. After pretreatment, a 5 vol%  $\text{CO}/\text{Ar}$  was periodically pulsed into the sample tube via a sampling valve with a loop of 100  $\mu\text{L}$ . For TPO, the spent catalyst (30 mg) was pretreated by 40  $\text{mL min}^{-1}$   $\text{Ar}$  at  $150^\circ\text{C}$  for 2 h and cooled down to  $40^\circ\text{C}$ . The sample was then heated from 40 to  $700^\circ\text{C}$  at a rate of  $5^\circ\text{C min}^{-1}$  in a 40  $\text{mL min}^{-1}$  of 20 vol%  $\text{O}_2/\text{Ar}$  flow. The effluent was monitored by recording the intensities of  $m/e = 28, 44, 18$ , and 20, and the amounts of  $\text{CO}$ ,  $\text{CO}_2$ , and  $\text{H}_2\text{O}$  were calculated using  $\text{Ar}$  as an internal standard. The contribution of the  $\text{CO}_2$  fragment to the signal of  $m/e = 28$  ( $\text{CO}$ ) was subtracted from the total intensity to get the actual amount of  $\text{CO}$ . The amount of coke was given by the sum of C and H atoms from  $\text{CO}$ ,  $\text{CO}_2$  and  $\text{H}_2\text{O}$ , and the H/C mole ratio was derived from their relative amount. In addition, the discharge gas during catalyst calcination was monitored on the same apparatus by recording the intensities of  $m/e = 17, 18, 28, 30, 44, 46$ , and 20.

Diffuse reflectance infrared Fourier transform spectroscopy (DRIFTS) data of  $\text{CO}$  adsorbed on the catalysts were collected on a Nicolet 6700 spectrometer equipped with a diffuse reflectance accessory and an MCT/A detector. A high-temperature cell connected to a gas flow control and vacuum system was used for an *in situ* pretreatment of the catalysts and the adsorption of  $\text{CO}$ . The sample was pretreated and then cooled to room temperature to record the background spectrum. After saturated adsorption of  $\text{CO}$  and adequate purging, the spectra were collected using 16 scans referenced to the background spectrum.

### 2.3. Catalytic test

Propane dehydrogenation reaction was carried out in a conventional fixed-bed reactor. The catalyst (200 mg) was loaded in a quartz tube. The sample was *in situ* prereduced under a 50  $\text{mL min}^{-1}$  of 10 vol%  $\text{H}_2/\text{N}_2$  at  $550^\circ\text{C}$  for 2 h. After reduction, the reaction gas mixture was introduced into the system. The gas mixture was composed of  $\text{C}_3\text{H}_8$ ,  $\text{H}_2$  and  $\text{N}_2$  with a molar ratio of 6:2:42 under ambient pressure and the gas hourly space velocity (GHSV) was  $15000 \text{ mL g}_{\text{cat}}^{-1} \text{ h}^{-1}$ . The outlet gas composition was analyzed by an online Agilent 7890A gas chromatography equipped with an FID detector and HP-Plot $\text{Al}_2\text{O}_3/\text{S}$  capillary column.

Propane conversion and propylene selectivity are defined as follows:

$$\text{Conversion (X)} = \frac{[\text{CH}_4] + 2[\text{C}_2\text{H}_4] + 2[\text{C}_2\text{H}_6] + 3[\text{C}_3\text{H}_6] + 4[\text{C}_4] + 6[\text{C}_6]}{[\text{CH}_4] + 2[\text{C}_2\text{H}_4] + 2[\text{C}_2\text{H}_6] + 3[\text{C}_3\text{H}_6] + 3[\text{C}_3\text{H}_8] + 4[\text{C}_4] + 6[\text{C}_6]} \times 100\%$$

$$\text{Selectivity(S)} = \frac{3[\text{C}_3\text{H}_6]}{[\text{CH}_4] + 2[\text{C}_2\text{H}_4] + 2[\text{C}_2\text{H}_6] + 3[\text{C}_3\text{H}_6] + 4[\text{C}_4] + 6[\text{C}_6]} \times 100\%$$

where  $[\text{C}_3\text{H}_8]$ ,  $[\text{C}_3\text{H}_6]$ ,  $[\text{C}_2\text{H}_6]$ ,  $[\text{C}_2\text{H}_4]$ ,  $[\text{CH}_4]$ ,  $[\text{C}_4]$ , and  $[\text{C}_6]$  refer to the concentration of outlet gas component. Almost no heavy component more than six carbon ( $\text{C}_{6+}$ ) could be detected. Note, coke on the catalysts is not included in the calculation of conversion and selectivity. Thus the realistic propane conversion is slightly higher and propylene selectivity is slightly lower than the values given by the above equations. However, based on the TPO analysis, the average coke selectivity during an 8 h run under our operation condition is generally no more than 1%, so the above equations is acceptable.

The first-order deactivation rate constant ( $K_d$ ) of catalysts is calculated by the following formula:

$$K_d = \frac{\ln(1/X_f - 1) - \ln(1/X_i - 1)}{t}$$

where  $X_i$  and  $X_f$  refer to the initial and the final conversion, respectively.

Periodic reaction-regeneration cycles were performed through coke-burning regeneration of the spent catalyst *in situ*. After each PDH reaction cycle of 8 h, the catalyst was cooled to room temperature with  $N_2$  purge, heated in 2 vol%  $O_2/N_2$  to 550 °C at a ramp of 5 °C min<sup>-1</sup> and held for 30 min, purged with  $N_2$  again, and then reduced in 10 vol%  $H_2/N_2$  at 550 °C for 1 h.

### 3. Results and discussion

#### 3.1. Comparison of Pt/Al<sub>2</sub>O<sub>3</sub> and Pt/BN

Fig. 1 shows the comparison of the Pt/Al<sub>2</sub>O<sub>3</sub> and Pt/BN in PDH. It can be found that the conversion of propane in the initial stage was almost identical over the Pt/Al<sub>2</sub>O<sub>3</sub> and Pt/BN, and it gradually dropped over both catalysts with time on stream (Fig. 1a). Obviously, the conversion of propane on the Pt/BN decreased more slowly than that on the Pt/Al<sub>2</sub>O<sub>3</sub>, indicating better stability of the Pt/BN. The first-order deactivation rate constant ( $K_d$ ) on the Pt/Al<sub>2</sub>O<sub>3</sub> and Pt/BN are 0.14 and 0.09 h<sup>-1</sup>, respectively (Fig. 1c). The less coke accumulation on the Pt/BN is responsible for its lower deactivation rate, as demonstrated by TPO (Fig. 1b). After an 8 h reaction, the coke content on the Pt/BN is 0.45 wt%, just a quarter of that on the Pt/Al<sub>2</sub>O<sub>3</sub> (1.73 wt%). Moreover, the H/C ratio of coke deposited on the Pt/Al<sub>2</sub>O<sub>3</sub> (1.04) is lower than that on the Pt/BN (1.33), suggesting that the acidity of the support leads to more hydrogen-deficient coke with lower mobility. In fact, it is generally accepted that there are two coking paths in PDH, the deep dehydrogenation and cracking from propane to the C atom and the polymerization of propylene [31]. The acid center on the support not only can catalyze the polymerization of propylene, but also is active for the dehydrogenation and cracking, forming coke precursors and thus leading to severe coke deposition. Compared with the acidic Al<sub>2</sub>O<sub>3</sub> support, nonacidic BN can effectively suppress coke formation.

The difference in propylene selectivity on the Pt/Al<sub>2</sub>O<sub>3</sub> and Pt/BN is impressive. The Pt/Al<sub>2</sub>O<sub>3</sub> displayed an initial propylene selectivity less than 90%, which gradually increased to 95% with the decreasing propane conversion after an 8 h reaction. This can be attributed to the modification effect on the active metal center induced by coke deposition. However, the Pt/BN showed a very high and stable propylene selectivity, which is close to 98% in the initial stage and more than 99% in most of reaction stages. Note, this high propylene selectivity usually exists on the catalysts that the geometric and/or electronic structure of Pt is modified by adding promoters. Therefore, we speculate that the high propylene selectivity on Pt/BN originates not only from the absence of acidity on BN support, but also from a certain kind of interaction between BN and Pt, which needs to further investigation.

#### 3.2. Effect of catalyst calcination and reduction

Every step in the catalyst synthesis process plays an important role in tuning the structural characteristics of the catalyst and in turn its activity, selectivity, and stability [32]. In particular, heat treatment procedures of supported Pt catalysts are critical in controlling Pt particle size and the interaction between Pt and support. For instance, a recent report [14] discovered that, compared with the conventional calcination and reduction process, the direct  $H_2$  reduction can lead to smaller Pt-Zn clusters encapsulated by silicalite-1 zeolite, resulting in high PDH performance. Thus, the effect of catalyst calcination and reduction on the Pt/BN catalyst was explored and is shown in Fig. 2.

It can be found that proper calcination before reduction significantly improved the catalytic performance of the Pt/BN (Fig. 2a). Elevating calcination temperatures favored both propane conversion and propylene selectivity in a range from non-calcined to 600 °C, while higher calcination temperatures (650–700 °C) caused very low propane conversion. After calcination, proper reduction treatment increased propane conversion with elevating reduction temperatures, but had almost no effect on propylene selectivity (Fig. 2b). Similarly, too high reduction temperature (650 °C) caused low propane conversion.

Fig. 2(d and e) give the XRD patterns of the Pt/BN subjected to different calcination and reduction. All of the Pt/BN catalysts display almost identical diffraction peaks of h-BN, indicating good thermal stability of the BN support. A weak diffraction peak at 39.7° ascribing to Pt(111) can be distinguished, and it strengthens slightly when the calcination temperature exceeds 600 °C (Fig. 2d), suggesting that high calcination temperatures result in Pt growth. The reduction that followed calcination has little effect on the Pt diffraction (Fig. 2e).

To further examine the effect of catalyst calcination and reduction on the Pt dispersion, we conducted the Pt particle size statistics based on the HAADF-STEM images (Figs. S1 and S2), and the average sizes of Pt are summarized in Fig. 2(c). Interestingly, almost all Pt/BN catalysts undergoing different calcination and reduction treatments have the similar Pt size, except that too high calcination or reduction temperatures lead to obvious Pt growth. It seems that the low Pt loading inhibited the high temperature aggregation of Pt to a certain extent. In combination with the reaction data, it can be found that the catalytic performance of the Pt/BN is not related to the Pt particle size.

Two representative catalysts, one underwent reduction only (denoted as Pt/BN-R), the other underwent calcination and reduction (Pt/BN-C&R), were selected for detailed investigation. Fig. 2(f) shows the CO-chemisorption and TPO results of the two catalysts, and PDH results are given again for convenient comparison. It can be found that the CO uptake on the Pt/BN-R is three times as large as that on the Pt/BN-C&R, indicating the direct reduction without calcination causes more exposed Pt active sites. However, it seems contradictory that the Pt/BN-R with more exposed Pt sites displayed lower propane conversion than the Pt/BN-C&R with fewer exposed Pt sites. The TPO result shows that the coke amount on the Pt/BN-R is 42% more than that on the Pt/BN-C&R. This is consistent with the lower propylene selectivity on the Pt/BN-R, since lower propylene selectivity means more cracking, which favors forming coke precursors. A previous report [33] has revealed that there are quick deactivation and steady states during PDH. The quick deactivation occurs because most of the active sites are occupied by cracking products which are hardly removed from the surface. It is most likely that the activity of the Pt/BN-R significantly decreased in the quick deactivation stage, in which the exposed Pt sites were largely occupied. As a result, the Pt/BN-R showed lower activity in the subsequent steady stage than the Pt/BN-C&R. Besides, in view of the similar Pt size on the Pt/BN-R and Pt/BN-C&R, the great difference in CO uptake on them seems abnormal. One possible explanation is that the Pt particles on the Pt/BN-C&R might be partially covered, resulting in its low CO uptake. It seems that the calcination treatment caused this covering of Pt on the Pt/BN-C&R.

#### 3.3. Calcination-induced and reduction-adjusted strong metal-support interactions

Recently, Dong et al. [23] reported a new type of reaction-induced SMSI between metals and BN nanosheets. They discovered that weak oxidizing gases such as CO<sub>2</sub> and H<sub>2</sub>O induce the encapsulation of Ni nanoparticles by ultrathin BO<sub>x</sub> overlayers derived

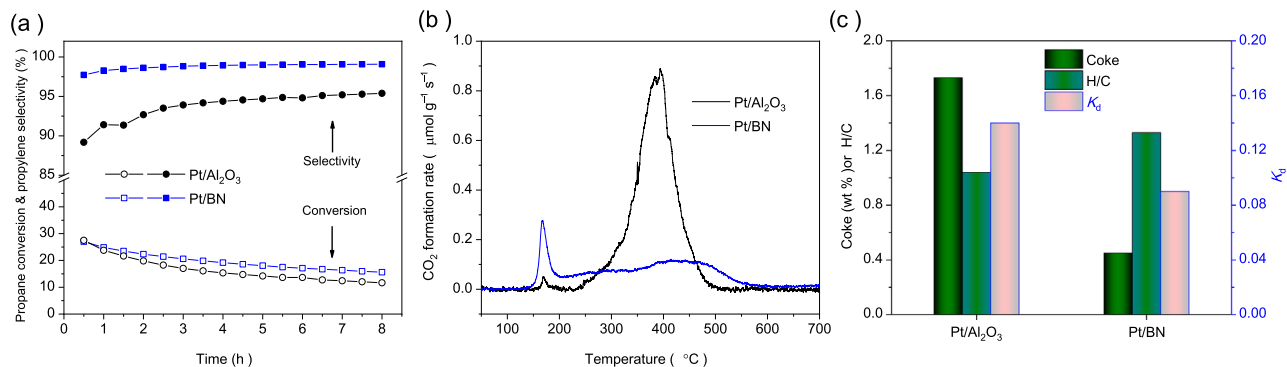


**Fig. 1.** Comparison of Pt/Al<sub>2</sub>O<sub>3</sub> and Pt/BN for propane dehydrogenation. (a) Time dependences of propane conversion and propylene selectivity over different catalysts. Reaction conditions: 0.2 g catalyst, C<sub>3</sub>H<sub>8</sub>:H<sub>2</sub>:N<sub>2</sub> = 6:2:42, GHSV = 15000 mL g<sub>cat</sub><sup>-1</sup>h<sup>-1</sup>, 540 °C, 0.1 MPa. (b) TPO profiles of the catalysts after an 8 h reaction. (c) First-order deactivation rate constant ( $K_d$ ) over different catalysts and the content and H/C ratio of the coke deposited on the catalysts after an 8 h reaction.

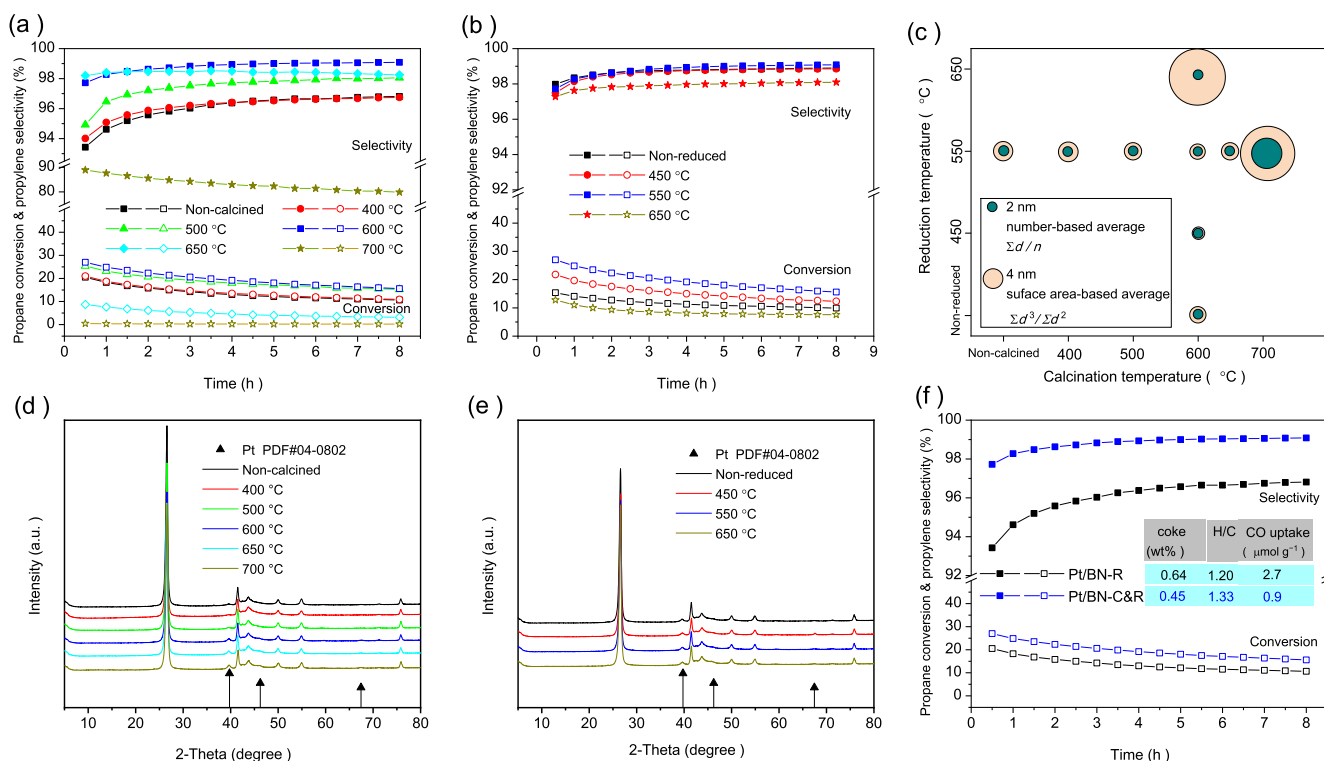
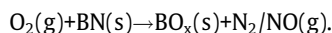


**Fig. 2.** Effect of catalyst calcination and reduction. Reaction conditions: 0.2 g catalyst, C<sub>3</sub>H<sub>8</sub>:H<sub>2</sub>:N<sub>2</sub> = 6:2:42, GHSV = 15000 mL g<sub>cat</sub><sup>-1</sup>h<sup>-1</sup>, 540 °C, 0.1 MPa. (a) Time dependences of propane conversion and propylene selectivity over the Pt/BN catalysts with different calcination temperatures. After calcination, all catalysts were reduced at 550 °C in a 10 vol% H<sub>2</sub>/N<sub>2</sub> flow. (b) Time dependences of propane conversion and propylene selectivity over the Pt/BN catalysts with different reduction temperatures. Before reduction, all catalysts were calcined at 600 °C in air. (c) Pt particle sizes from HAADF-STEM (Figs. S1 and S2). (d and e) XRD patterns. (f) Comparison of the representative catalysts. Pt/BN-R stands for the catalyst that only underwent reduction at 550 °C, and Pt/BN-C&R stands for the catalyst undergoing calcination at 600 °C and reduction at 550 °C. The inset shows CO uptake over different catalysts from pulse chemisorption and the content and H/C ratio of the coke deposited on the catalysts after an 8 h reaction.

from oxidative etching of the h-BN support during the dry reforming of methane at 750 °C. They also found that the noble metal Pt oxidative etching of h-BN occurs under O<sub>2</sub> atmosphere instead of CO<sub>2</sub> or H<sub>2</sub>O. Along with the etching of h-BN, the amorphous BO<sub>x</sub> overlayers cover the surface of Pt nanoparticles supported on the BN nanosheets after the treatment in 21% O<sub>2</sub>/Ar at 800 °C for 2 h. We speculate that a similar SMSI exists on our Pt/BN catalysts after calcination treatment, and the resulting BO<sub>x</sub> overlayers covering Pt lead to low CO uptake on the Pt/BN-C&R. Therefore, some characterizations were conducted to verify this speculation.

The discharge gas during catalyst calcination was monitored, as shown in Fig. 3(a). It can be observed that the release of NO<sub>x</sub> derived from the oxidative decomposition of the Pt(NH<sub>3</sub>)<sub>4</sub>(NO<sub>3</sub>)<sub>2</sub>

precursor under O<sub>2</sub> atmosphere occurs in 180–280 °C, while the release of H<sub>2</sub>O continues to 500 °C. An extra nitric oxide peak and the remarkable increase of nitrogen signal can be observed when the calcination temperature exceeds 520 °C, suggesting the oxidative etching of the BN support and the formation of BO<sub>x</sub> during calcination. This process can be described by the formula



In a control experiment under H<sub>2</sub> atmosphere, the reduction and decomposition of the Pt(NH<sub>3</sub>)<sub>4</sub>(NO<sub>3</sub>)<sub>2</sub> precursor occur below 250 °C, and ammonia is the major N-containing product. Nothing else happened during the direct reduction treatment. Fig. 3(b) shows the HRTEM image of the Pt/BN-R, in which clear boundary



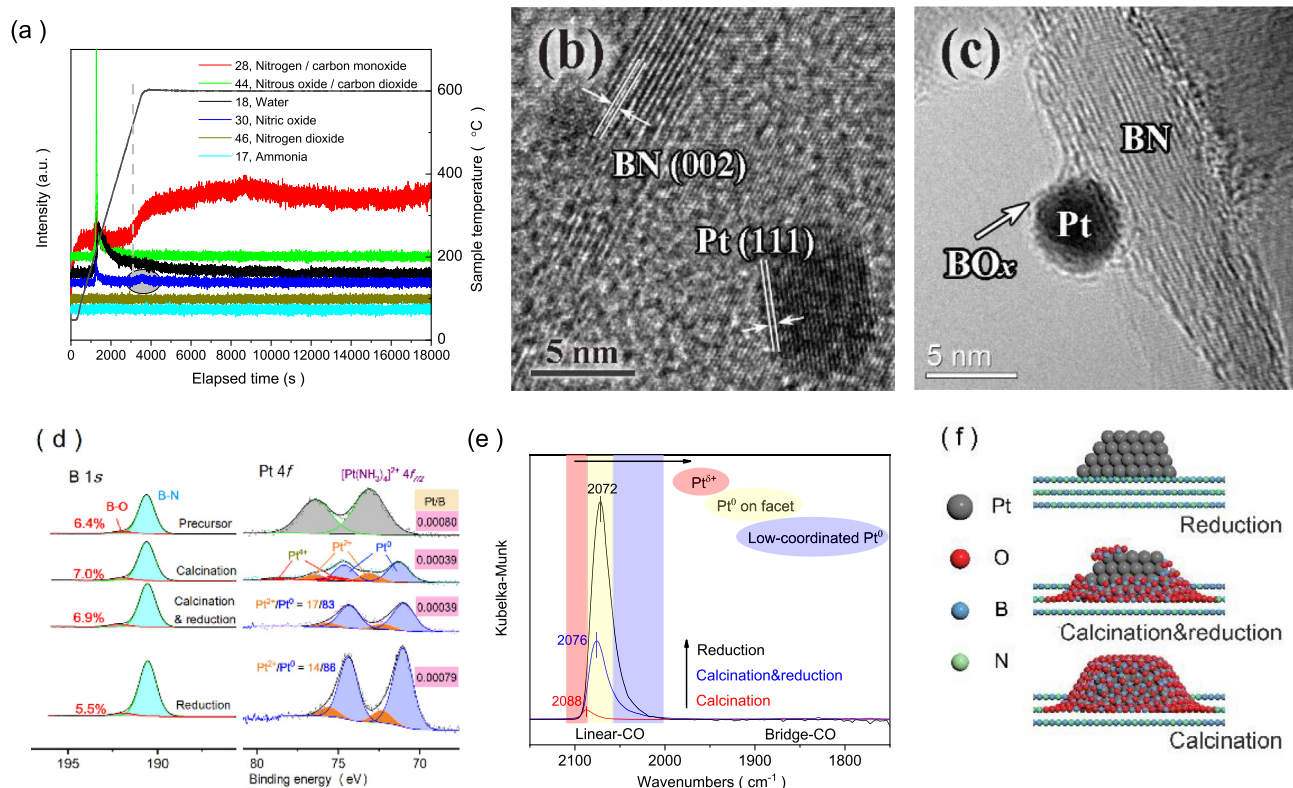


**Fig. 3.** Calcination-induced and reduction-adjusted strong metal-support interactions between Pt and BN. (a) MS monitoring of discharge gas during catalyst calcination under 20 vol% O<sub>2</sub>/Ar atmosphere. (b) HRTEM images of Pt/BN-R. (c) HRTEM images of Pt/BN-C&R. (d) B 1s and Pt 4f XPS. (e) CO-DRIFTS. (f) Illustration of bare Pt particles on Pt/BN-R without SMSI, partial encapsulation of Pt particles by BO<sub>x</sub> overlayers on Pt/BN-C&R with controlled SMSI, and complete encapsulation of small Pt particles by BO<sub>x</sub> overlayers on Pt/BN-C with SMSI. R and C stand for the catalyst undergoing calcination and reduction, respectively.

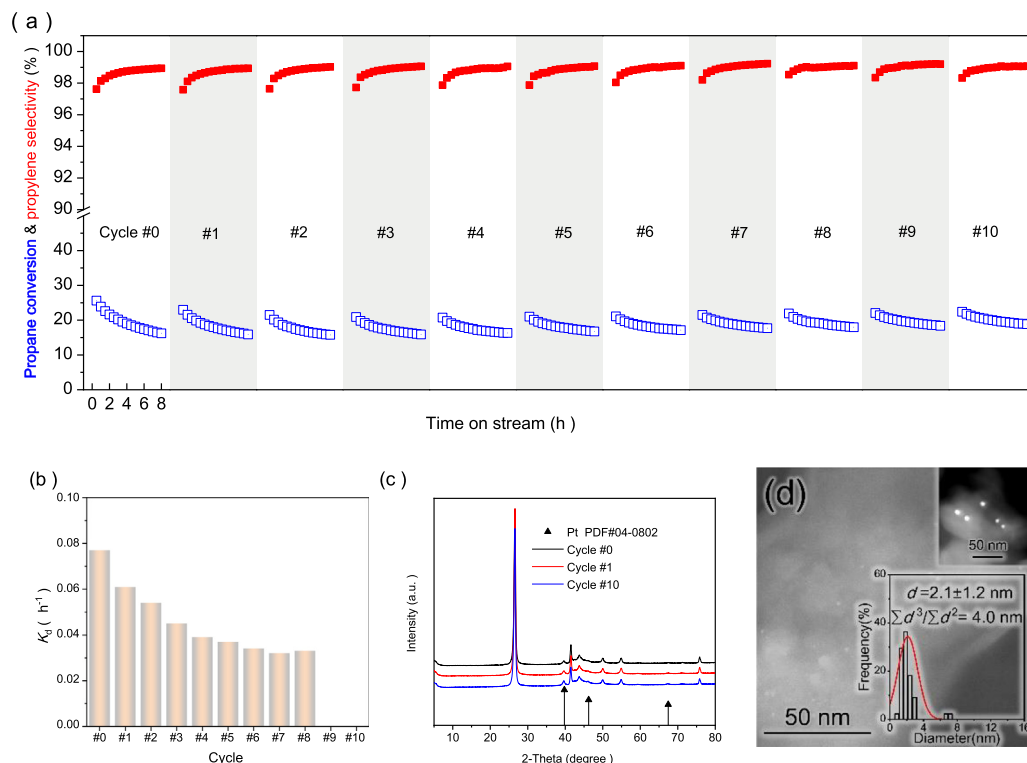
of Pt particle supported on the BN support can be observed. Instead, the partial encapsulation of Pt particle by calcination-induced BO<sub>x</sub> overlayers can be observed on the Pt/BN-C&R (Fig. 3c).

Fig. 3(d) shows the B 1s and Pt 4f XPS of the Pt/BN catalyst undergoing *in situ* calcination and/or reduction treatment. The surface Pt/B ratio on the Pt/BN-C (0.00039) or Pt/BN-C&R (0.00039) is much lower than that on the precursor (0.00080) or Pt/BN-R (0.00079), which is in accordance with the encapsulation of Pt by calcination-induced BO<sub>x</sub> overlayers. The B 1s spectra were fitted into two components, B–O at 192.0 eV and B–N at 190.6 eV. For the precursor, the percentage of B–O component is 6.4%. It can be found that the percentage of B–O component decreased after reduction (5.5%), while it increased after calcination (7.0%), further confirming the formation of BO<sub>x</sub> species during calcination. The subsequent reduction after calcination just caused a very slight decrease in the percentage of B–O component (6.9%), implying that most of the BO<sub>x</sub> overlayers are retained. Moreover, the fitting of Pt 4f spectra gives the Pt valence state composition. After calcination, most of Pt<sup>0</sup> and a few of Pt<sup>2+</sup> and Pt<sup>4+</sup> coexist on the Pt/BN-C. The subsequent reduction makes more Pt species convert into the metallic state on the Pt/BN-C&R. Compared with the direct reduction (Pt/BN-R), the reduction after calcination (Pt/BN-C&R) retains more Pt<sup>2+</sup> component, which is related to the BO<sub>x</sub> overlayers on the Pt/BN-C&R. Meanwhile, due to the low melting points of boron oxides (around 400 °C) [23], the liquid-like BO<sub>x</sub> overlayers are likely to be partially redistributed to form defects and pores along with the reduction of Pt species. As a result, the calcination-induced encapsulation of Pt can be adjusted by the subsequent reduction, showing better accessibility of Pt. A typical SMSI on Pt/TiO<sub>2</sub> undergoing high-temperature reduction often has a partially reduced TiO<sub>x</sub> layer covering Pt, which may result in active site blocking. Macino

et al. [32] discovered that the SMSI on Pt/TiO<sub>2</sub> can be restrained by adding a calcination process before catalyst reduction, which decreases the coverage of TiO<sub>x</sub> over Pt nanoparticles. Interestingly, in our case, the calcination and reduction displays opposite effects. The calcination induces the SMSI and the encapsulation of Pt, whereas the reduction after catalyst calcination can not only further convert Pt into metallic state but also adjust the SMSI by the redistribution of BO<sub>x</sub> overlayers. The structural models of Pt/BN catalysts undergoing different treatments are shown in Fig. 3(f) based on the above analysis.

Note, the formation of Pt–B alloy cannot be supported by the present XPS results because the metallic Pt species did not obviously shift to lower binding energy. Thus, we believe that the geometric effect of the BO<sub>x</sub> overlayers on the encapsulated Pt is essential for the outstanding propylene selectivity on the Pt/BN-C&R. For the Pt/BN-R without calcination-induced SMSI, the direct reduction leads to the formation of bare Pt particles including large amount of low-coordinated Pt sites, which are very active in C–H and C–C bond activation and prone to deep reaction [31], causing more cracking and coking and in turn lower propylene selectivity. However, the calcination-induced and reduction-adjusted SMSI between Pt and BN results in partial encapsulation of Pt particles by BO<sub>x</sub> overlayers on the Pt/BN-C&R. The BO<sub>x</sub> overlayers might block the low-coordinated Pt sites and constrain Pt particles into smaller ensembles, causing high propylene selectivity.

The CO-DRIFTS were conducted to further investigate the structural and electronic properties of Pt on the Pt/BN catalysts undergoing different treatments. As shown in Fig. 3(e), no absorption band assigned to bridge-adsorbed CO on large Pt particles (~1850 cm<sup>-1</sup>) can be observed, suggesting the small-sized Pt particles on all samples. The linear-adsorbed CO contains three com-



**Fig. 4.** Cyclic stability test of the Pt/BN-C&R catalyst for propane dehydrogenation. Reaction conditions: 0.2 g catalyst,  $\text{C}_3\text{H}_8:\text{H}_2:\text{N}_2 = 6:2:42$ , GHSV =  $15000 \text{ mL g}_{\text{cat}}^{-1} \text{h}^{-1}$ ,  $540^\circ\text{C}$ , 0.1 MPa; after each reaction cycle of 8 h, the catalyst was cooled to room temperature with  $\text{N}_2$  purge, heated in 2 vol%  $\text{O}_2/\text{N}_2$  to  $550^\circ\text{C}$  at a ramp of  $5^\circ\text{C min}^{-1}$  and held for 30 min, purged with  $\text{N}_2$  again, and then reduced in 10 vol%  $\text{H}_2/\text{N}_2$  at  $550^\circ\text{C}$  for 1 h. (a) Propane conversion and propylene selectivity during periodic reaction-regeneration cycles. (b) First-order deactivation rate constant ( $K_d$ ) over each reaction cycle. (c) XRD patterns. (d) Typical HAADF-STEM image of the Pt/BN-C&R catalyst after 10 reaction-regeneration cycles and the corresponding Pt particle size statistics. The upper-right inset shows large Pt particles that were found occasionally.

ponents with gradual red shift of absorption band, CO adsorbed on  $\text{Pt}^{\delta+}$ , on facet  $\text{Pt}^0$ , and on low-coordinated  $\text{Pt}^0$  [34]. It can be found that the calcination alone leads to a very low amount of CO adsorbed on  $\text{Pt}^{\delta+}$ , the calcination and reduction result in a medium amount of CO mainly adsorbed on facet  $\text{Pt}^0$ , and the reduction alone causes a large amount of CO adsorbed on  $\text{Pt}^0$ , which contains more low-coordinated  $\text{Pt}^0$  sites. Obviously, the existence of  $\text{BO}_x$  overlayers derived from calcination blocks CO adsorption on Pt, and the subsequent reduction weakens the blocking, leading to more CO adsorption. This is well consistent with the structural models of Pt/BN catalysts shown in Fig. 3(f) and reinforces the idea that the geometric effect of the  $\text{BO}_x$  overlayers on the encapsulated Pt is responsible for the high propylene selectivity on the Pt/BN-C&R.

### 3.4. Cyclic stability test

Coke deposition and Pt sintering are the key issues for the deactivation of Pt-based catalysts in PDH. We have confirmed that the Pt/BN can effectively suppress coke formation due to the absence of acidity on BN support, and the calcination-induced SMSI between Pt and BN causes the encapsulation of Pt particles by  $\text{BO}_x$  overlayers, which further suppress coke formation. So, the Pt/BN displays better single-pass stability in PDH than the Pt/ $\text{Al}_2\text{O}_3$  (Fig. 1). However, the coke deposition in PDH is inevitable, so periodic or continuous catalyst regeneration is necessary for achieving a sufficient total lifetime. Considering that the  $\text{BO}_x$  overlayers probably inhibit Pt sintering by the spatial isolation, the Pt/BN-C&R is supposed to be highly stable in both PDH reaction and regeneration.

The periodic reaction-regeneration cycles were performed through coke-burning regeneration of the spent catalyst *in situ*,

and the cyclic stability test results are shown in Fig. 4. As expected, the Pt/BN-C&R shows very high stability (Fig. 4a). It can be found that the initial conversion of propane decreased slightly in the early four cycles, but increased in the following cycles, displaying a typical catalyst maturation process. This is also confirmed by the gradual decrease in the deactivation rate constant for each cycle (Fig. 4b). It seems that the calcination and reduction during the periodic coke-burning regeneration process further modify and stabilize the structure of the catalyst. Almost no change can be observed in the XRD patterns of the Pt/BN subjected to different reaction-regeneration cycles (Fig. 4c), indicating the structural stability of the Pt/BN. The HRTEM shows that the average size of Pt particles on the Pt/BN after ten reaction-regeneration cycles (Fig. 4d) just increased very slightly compared with that on the fresh sample (Fig. 2c and Fig. S1). Instead, previous study [35] discovered that the same reaction-regeneration cycles can lead to severe Pt sintering on  $\text{Al}_2\text{O}_3$  support, even if Sn promoter is added. This suggests that the spatial isolation of Pt by the calcination-induced  $\text{BO}_x$  overlayers can effectively inhibit Pt sintering. Therefore, the Pt/BN catalyst displays high sintering resistance and cyclic stability in PDH.

## 4. Conclusions

We have demonstrated that h-BN is a promising support of Pt-based catalysts for PDH reaction. The Pt/BN catalyst undergoing calcination and reduction is highly stable in PDH reaction and coke-burning regeneration, together with low coke deposition and outstanding propylene selectivity. It has been revealed that the high coke resistance and high propylene selectivity of the Pt/BN catalyst are derived not only from the absence of acidity on

BN support, but also from the calcination-induced and reduction-adjusted SMSI between Pt and BN, which causes the partial encapsulation of Pt particles by  $\text{BO}_x$  overlayers. The  $\text{BO}_x$  overlayers can block the low-coordinated Pt sites and constrain Pt particles into smaller ensembles, suppressing side reactions such as cracking and deep dehydrogenation. Moreover, the  $\text{BO}_x$  overlayers can effectively inhibit Pt sintering by the spatial isolation of Pt during periodic reaction-regeneration cycles. In this work, the catalyst support for PDH is expanded to nonoxide BN, and the understanding of SMSI between Pt and BN will provide rational design strategy for BN-based catalysts.

### Declaration of Competing Interest

The authors declare that they have no known competing financial interests or personal relationships that could have appeared to influence the work reported in this paper.

### Acknowledgments

This work was financially supported by the National Natural Science Foundation of China (21273049, 22172037), the Guangdong Basic and Applied Basic Research Foundation (2021A1515010014), the Science and Technology Program of Guangzhou (201904010023) and the CAS Key Laboratory of Renewable Energy (E029kf0901). We also thank Dr. Kai Yan of GDUT Analysis and Test Center for the *in situ* treatment of samples in XPS measurements.

### Appendix A. Supplementary data

Supplementary data to this article can be found online at <https://doi.org/10.1016/j.jechem.2021.10.008>.

### References

- [1] J.J.H.B. Sattler, J. Ruiz-Martinez, E. Santillan-Jimenez, B.M. Weckhuysen, *Chem. Rev.* 114 (2014) 10613–10653.
- [2] Z. Nawaz, *Rev. Chem. Eng.* 31 (2015) 413–436.
- [3] Z.P. Hu, D. Yang, Z. Wang, Z.Y. Yuan, *Chin. J. Catal.* 40 (2019) 1233–1254.
- [4] Y.H. Dai, X. Gao, Q.J. Wang, X.Y. Wan, C.M. Zhou, Y.H. Yang, *Chem. Soc. Rev.* 50 (2021) 5590–5630.
- [5] E.E. Stangland, *Annu. Rev. Chem. Biomol. Eng.* 9 (2018) 341–364.
- [6] R. Ryoo, J. Kim, C. Jo, S.W. Han, J.C. Kim, H. Park, J. Han, H.S. Shin, J.W. Shin, *Nature* 585 (2020) 221–224.
- [7] A.H. Motagamwala, R. Almallahi, J. Wortman, V.O. Igenegbai, S. Linic, *Science* 373 (2021) 217–222.
- [8] H. Yan, K. He, I.A. Samek, D. Jing, M.G. Nanda, P.C. Stair, J.M. Notestein, *Science* 371 (2021) 1257–1260.
- [9] H. Zhou, X.F. Yi, Y. Hui, L. Wang, W. Chen, Y.C. Qin, M. Wang, J.B. Ma, X.F. Chu, Y. Q. Wang, X. Hong, Z.F. Chen, X.J. Meng, H. Wang, Q.Y. Zhu, L.J. Song, A.M. Zheng, F.S. Xiao, *Science* 372 (2021) 76–80.
- [10] L. Nykanen, K. Honkala, *ACS Catal.* 3 (2013) 3026–3030.
- [11] H.B. Zhu, D.H. Anjum, Q.X. Wang, E. Abou-Hamad, L. Emsley, H.L. Dong, P. Laveille, L.D. Li, A.K. Samal, J.M. Basset, *J. Catal.* 320 (2014) 52–62.
- [12] L.C. Liu, M. Lopez-Haro, C.W. Lopes, C.G. Li, P. Concepcion, L. Simonelli, J.J. Calvino, A. Corma, *Nat. Mater.* 18 (2019) 866–873.
- [13] L.C. Liu, M. Lopez-Haro, C.W. Lopes, S. Rojas-Buzo, P. Concepcion, R. Manzorro, L. Simonelli, A. Sattler, P. Serna, J.J. Calvino, A. Corma, *Nat. Catal.* 3 (2020) 628–638.
- [14] Q.M. Sun, N. Wang, Q.Y. Fan, L. Zeng, A. Mayoral, S. Miao, R.O. Yang, Z. Jiang, W. Zhou, J.C. Zhang, T.J. Zhang, J. Xu, P. Zhang, J. Cheng, D.C. Yang, R. Jia, L. Li, Q.H. Zhang, Y. Wang, O. Terasaki, J.H. Yu, *Angew. Chem. Int. Ed.* 59 (2020) 19450–19459.
- [15] S. Chen, Z.J. Zhao, R.T. Mu, X. Chang, J. Luo, S.C. Purdy, A.J. Kropf, G.D. Sun, C.L. Pei, J.T. Miller, X.H. Zhou, E. Vovk, Y. Yang, J.L. Gong, *Chemistry* 7 (2021) 387–405.
- [16] O.B. Belskaya, L.N. Stepanova, T.I. Gulyaeva, S.B. Erenburg, S.V. Trubina, K. Kvashnina, A.I. Nizovskii, A.V. Kalinkin, V.I. Zaikovskii, V.I. Bukhtiyarov, V.A. Likholobov, *J. Catal.* 341 (2016) 13–23.
- [17] S.W. Han, H. Park, J. Han, J.-C. Kim, J. Lee, C. Jo, R. Ryoo, *ACS Catal.* (2021) 9233–9241.
- [18] Y.R. Zhu, Z. An, H.Y. Song, X. Xiang, W.J. Yang, J. He, *ACS Catal.* 7 (2017) 6973–6978.
- [19] C.A. Lin, J.C.S. Wu, J.W. Pan, C.T. Yeh, *J. Catal.* 210 (2002) 39–45.
- [20] J.C.S. Wu, C.Y. Chen, S.D. Lin, *Catal. Lett.* 102 (2005) 223–227.
- [21] J.C.S. Wu, H.C. Chou, *Chem. Eng. J.* 148 (2009) 539–545.
- [22] Y.R. Liu, X. Li, W.M. Liao, A.P. Jia, Y.J. Wang, M.F. Luo, J.Q. Lu, *ACS Catal.* 9 (2019) 1472–1481.
- [23] J.H. Dong, Q. Fu, H.B. Li, J.P. Xiao, B. Yang, B.S. Zhang, Y.X. Bai, T.Y. Song, R.K. Zhang, L.J. Gao, J. Cai, H. Zhang, Z. Liu, X.H. Bao, *J. Am. Chem. Soc.* 142 (2020) 17167–17174.
- [24] L.J. Gao, Y. Wang, H.B. Li, Q.H. Li, N. Ta, L. Zhuang, Q. Fu, X.H. Bao, *Chem. Sci.* 8 (2017) 5728–5734.
- [25] M.M. Sun, Q. Fu, L.J. Gao, Y.P. Zheng, Y.Y. Li, M.S. Chen, X.H. Bao, *Nano Res.* 10 (2017) 1403–1412.
- [26] W. Bi, Y.J. Hu, H. Jiang, L. Zhang, C.Z. Li, *Adv. Funct. Mater.* 26 (2021) 2010780.
- [27] J.T. Grant, C.A. Carrero, F. Goeltl, J. Venegas, P. Mueller, S.P. Burt, S.E. Specht, W. P. McDermott, A. Chiericato, I. Hermans, *Science* 354 (2016) 1570–1573.
- [28] L. Shi, D.Q. Wang, W. Song, D. Shao, W.P. Zhang, A.H. Lu, *Chemcatchem* 9 (2017) 1788–1793.
- [29] H. Fu, K. Huang, G. Yang, Y. Cao, H. Wang, F. Peng, X. Cai, H. Gao, Y. Liao, H. Yu, *ACS Catal.* 11 (2021) 8872–8880.
- [30] Z. Cao, J. Bu, Z. Zhong, C. Sun, Q. Zhang, J. Wang, S. Chen, X. Xie, *Appl. Catal. A-Gen.* 578 (2019) 105–115.
- [31] Z. Lian, C. Si, F. Jan, S. Zhi, B. Li, *ACS Catal.* 11 (2021) 9279–9292.
- [32] M. Macino, A.J. Barnes, R.Y. Qu, E.K. Gibson, D.J. Morgan, S.J. Freakley, N. Dimitratos, C.J. Kiely, X. Gao, A.M. Beale, D. Bethell, Q. He, M. Sankar, G.J. Hutchings, S.M. Althabban, *Nat. Catal.* 2 (2019) 873–881.
- [33] Z. Lian, S. Ali, T. Liu, C. Si, B. Li, D.S. Su, *ACS Catal.* 8 (2018) 4694–4704.
- [34] Q.S. Zhang, J.H. Bu, J.D. Wang, C.Y. Sun, D.Y. Zhao, G.Z. Sheng, X.W. Xie, M. Sun, L. Yu, *ACS Catal.* 10 (2020) 10350–10363.
- [35] C.Y. Sun, J.Y. Luo, M.J. Cao, P. Zheng, G.C. Li, J.H. Bu, Z. Cao, S.H. Chen, X.W. Xie, *J. Energy Chem.* 27 (2018) 311–318.